



# Structure–activity relation of iron oxide catalysts in soot oxidation

Steffen Wagloehner<sup>a</sup>, Julian N. Baer<sup>b</sup>, Sven Kureti<sup>a,\*</sup>

<sup>a</sup> Technical University of Freiberg, Department of Energy Process Engineering and Chemical Engineering, Fuchsmuehlenweg 9, D-09596 Freiberg, Germany

<sup>b</sup> Karlsruhe Institute of Technology, Institute for Chemical Technology and Polymer Chemistry, Kaiserstr. 12, D-76131 Karlsruhe, Germany



## ARTICLE INFO

### Article history:

Received 17 May 2013

Received in revised form 7 September 2013

Accepted 28 September 2013

Available online 9 October 2013

### Keywords:

Structure–activity correlation

Iron oxide

Soot oxidation

Kinetic modelling

NH<sub>3</sub> adsorption and desorption

## ABSTRACT

In this paper, a systematic series of bare iron oxide catalysts was evaluated towards their activity for the oxidation of soot under oxygen-rich conditions. The catalytic studies were performed by temperature programmed oxidation (TPO) using tight contact mixtures of catalyst and soot. A home-made carbon black originated from propene combustion was taken as model soot. The catalysts were thoroughly characterised by employing powder X-ray diffraction (PXRD), N<sub>2</sub> physisorption, high resolution transmission electron microscopy (HRTEM), temperature programmed reduction by H<sub>2</sub> (HTPR), temperature programmed desorption of NH<sub>3</sub> (NH<sub>3</sub>-TPD), temperature programmed desorption of O<sub>2</sub> (O<sub>2</sub>-TPD) and thermogravimetry coupled with difference thermal analysis (TG/DTA). Special notice was put on the NH<sub>3</sub>-TPD data, which were used for the modelling of the NH<sub>3</sub> adsorption and desorption. This model included elementary reactions and implied the specific number of Bronsted and Lewis acid sites. The obtained kinetic parameters were found to be close to that of related oxides such as ZrO<sub>2</sub> and H-BEA zeolite. The results of the physical–chemical characterisation as well as NH<sub>3</sub> adsorption/desorption kinetics were coupled with the catalytic performance to identify determining properties of the iron oxide catalysts. From these correlations it was derived that both Lewis acid surface sites as well as crystallinity drive the catalytic activity for soot oxidation. The effect of these characteristics is in line with the postulated role of the catalyst implying the transport of oxygen from iron oxide to soot by surface and bulk diffusion.

© 2013 Elsevier B.V. All rights reserved.

## 1. Introduction

Diesel engines are the most effective drive units implying increased fuel economy and reduced CO<sub>2</sub> emission. However, diesel engines represent an important source of soot particles, which reveal carcinogenic potential [1] and contribute to the greenhouse effect [2]. For the abatement of soot, so-called diesel particulate filters (DPF) were widely introduced for vehicles and working machines since a couple of years [3]. These filter systems operate in the wall flow mode implying the deposition of particles onto the porous filter walls, while the exhaust flows through them. But, the trapped soot accumulates in the DPF channels resulting in backpressure, which potentially decreases the engine efficiency. Therefore, a regeneration step is mandatory. For heavy duty diesels, the CRT technique (continuously regenerating trap) is applied, which involves the continuous oxidation of the trapped soot by NO<sub>2</sub> and O<sub>2</sub> [4]. The required NO<sub>2</sub> can be produced by the precious metal based diesel oxidation catalyst (DOC) located upstream to the DPF and by a catalytic Pt coating of the filter. However, CRT does not work efficiently in diesel passenger cars as single technique due to the low NO<sub>x</sub>/soot ratio [5]. Hence, common strategies include the post-injection of fuel leading to the emission of huge

amounts of hydrocarbons, CO and H<sub>2</sub>. These components are subsequently oxidised on the DOC resulting in steep temperature raise of the exhaust causing the soot to combust [6]. Another approach applied in practice is the use of fuel borne catalysts (FBC), for example ceria based organyls. FBC reduce the soot output of the engine and are embedded in the emitted particles thus enhancing the soot oxidation in the DPF [6].

Furthermore, the ignition temperature of soot can be reduced by the CDPF technique, which includes a catalytic DPF coating supporting the soot/O<sub>2</sub> reaction. The efficiency of this process is closely associated with tight contact between soot and catalytic coating. Indeed, in CDPF loose contact mostly predominates and therefore the catalysts developed so far show a rather limited benefit under practical conditions [7]. A variety of materials, mainly transition metal oxides [8–11] as well as rare earth metals oxides [11–15], basically reveals catalytic performance for the oxidation of soot. However, with regard to the rising demand of environmental catalysts, the use of rare catalytic components is problematic due to possible shortage of their raw materials. In this context, iron oxides are promising catalysts being associated with their natural availability and high activity for soot oxidation [16–18].

Some studies were reported on the mechanism of crystalline ferric oxide in the oxidation of soot [16,17,19]. For  $\alpha$ -Fe<sub>2</sub>O<sub>3</sub> it was shown that the transfer of oxygen from the catalyst to soot mainly occurs by physical contact points. One transfer route follows the

\* Corresponding author. Tel.: +49 3731 39 4482; fax: +49 3731 39 4555.

E-mail address: [kureti@iec.tu-freiberg.de](mailto:kureti@iec.tu-freiberg.de) (S. Kureti).

migration of oxygen from the catalyst lattice to the soot, while the formed vacancies are refilled by gaseous  $O_2$ . In another route, oxygen is “pumped” from the gas-phase via the  $Fe_2O_3$  surface to the soot. Furthermore, it has to be considered that the soot oxidation is a strongly exothermic reaction and therefore the local heat production is a crucial parameter of the oxidation kinetics. For  $Fe_2O_3$ /soot mixtures, it was demonstrated that the local temperature depends on the amount and heat capacity of the catalyst buffering the temperature. Thus, two opposite features exist, i.e. rising amount of the catalyst increases the number of contact points accelerating the soot oxidation on the one hand, but on the other hand it inclines the heat capacity limiting the reaction rate [20]. As a consequence, an optimum quantity of catalyst is required.

Furthermore, it should be stated that iron oxide catalysts enhance the direct soot/ $NO$  reaction to yield  $N_2$  and  $CO_x$ , whereas under oxygen-rich conditions the  $NO$  reduction represents rather a side reaction of the soot/ $O_2$  conversion [21,22]. Also, it has been recently reported that soot supports the  $NO_x$  reduction by  $NH_3$  [23], whereas it inhibits the uptake capacity of  $NO_x$  storage reduction catalysts [24].

Iron oxides exist in the form of oxide-hydroxides, hydroxides and oxides. The thermodynamically most stable modifications addressing typical reaction conditions of soot oxidation are  $\gamma$ - $Fe_2O_3$ ,  $Fe_3O_4$  and  $\alpha$ - $Fe_2O_3$ , whereas the latter is favoured up to 1500 °C [25]. The aim of this work was the investigation of the structure–activity relationship of the above-mentioned iron oxides for soot oxidation. Therefore, the catalysts were tested towards their activity and were physical-chemically characterised to obtain knowledge on acid surface sites, specific surface area, particle size, oxygen storage capacity and phase composition.

## 2. Experimental

### 2.1. Preparation and characterisation of catalysts and soot

Seven different iron oxides catalysts were examined implying three home-made and four commercial samples. The later ones are nano-sized patterns from Chempur (“10–20 nm” and “7–10 nm”) and Lanxess (“Bayoxide E 1.1” and “Bayoxide E 2.1”). They are denoted throughout this paper as C10-20, C7-10, E 1.1 and E 2.1.

The preparation procedures of the home-made samples were already reported elsewhere and are therefore only briefly described. The polyvinyl alcohol (PVA) route was used for the synthesis of bulk  $\alpha$ - $Fe_2O_3$  termed as PVA- $Fe_2O_3$  [26]; two aqueous solutions of iron nitrate and PVA were mixed, dried and finally calcined in static air at 600 °C for 5 h. The second sample is a  $\gamma$ - $Fe_2O_3$ . This catalyst was produced by using an aqueous solution of  $FeCl_2$  and  $FeCl_3$  precipitated at pH 7 at room temperature [27]. The precipitate was washed several times with deionised water, while a heat treatment was not required. XRF analysis of the sample showed a minor Cl content of ca. 0.15 wt.% only indicating sufficient washing. Nano-sized  $Fe_2O_3$  particles were prepared by flame-spray pyrolysis taking a 0.5 M aqueous  $Fe(NO_3)_3$  solution mixed with ethanol in the volume ratio of 1:4 [28]. This solution was sprayed and combusted by a two-substance nozzle (Duesen-Schlick) and the formed particles (FSP- $Fe_2O_3$ ) were collected by a sinter metal candle filter.

All the catalysts were physical-chemically characterised by a series of analytical tools. The crystalline structure was investigated by PXRD (powder X-ray diffraction). These analyses were done at room temperature on a D8 Advance diffractometer from Bruker-AXS with  $Co-K\alpha$  radiation (35 kV/45 mA) and Goebel mirror in 2 $\theta$  mode. The diffractograms were recorded from 10° to 80° with a step width of 0.0164° and a time of 0.05 s per step. Quantitative analyses were carried out by TOPAS software employing an

implemented standard fitting procedure according to the Rietveld refinement [29]

The Lewis and Bronsted acid sites and oxygen storage were examined by  $O_2$  and  $NH_3$ -TPD (temperature programmed desorption), respectively. For these analyses, the respective sample was pressed into pellets at a pressure of 4 MPa, granulated and sieved to a size of 125–250  $\mu$ m. Before TPD, the catalyst was fixed in the reactor by quartz wool and was pre-treated in  $N_2$  flow at 250 °C for 15 min to eliminate possible impurities, e.g.  $H_2O$  and  $CO_2$ , thus supplying reproducible conditions. Higher pre-treatment temperature was not adjusted to avoid sintering of nano-sized samples. After this, it was cooled down to 50 °C for  $NH_3$ -TPD and to 200 °C for  $O_2$ -TPD followed by  $NH_3$  and  $O_2$  exposure, respectively. After saturation, the catalyst was flushed with  $N_2$ , and the temperature was increased at a rate of 10 K min<sup>−1</sup>. The total gas flow was 500 ml min<sup>−1</sup> (STP), while temperature was monitored by a K-type thermocouple installed directly in front of the sample.  $NH_3$ -TPD was performed in quartz glass tube (i.d. 8 mm), whereas the sample was exposed to 500 ppm  $NH_3$  balanced by  $N_2$  (Air Liquide).  $NH_3$  was monitored by non-dispersive infrared spectroscopy (NDIR) using a BINOS 1.b from Leybold-Heraeus.  $O_2$ -TPD was carried out in a quartz glass tube (i.d. 10 mm). For saturation, a blend of  $O_2$  (500 ppm) and  $N_2$  balance (Air Liquide) was taken, while TPD was performed up to 700 °C.  $O_2$  was analysed by chemical ionisation mass spectrometry (CIMS, Airsense 500 from V&F).

HTPR analyses (temperature programmed reduction by  $H_2$ ) were performed to investigate the redox properties and the composition of the samples. 60 mg of catalyst powder was charged into the quartz glass tube reactor (i.d. 6 mm) and fixed with quartz wool. Then the reaction mixture (5 vol.%  $H_2$ , 95 vol.% Ar) was added with a flow of 200 ml min<sup>−1</sup> (STP), and the temperature was increased to 900 °C at a rate of 15 K min<sup>−1</sup>. The temperature was monitored by a K-type thermocouple located directly in front of the sample. The concentration of  $H_2$  was measured continuously with a Cirrus mass spectrometer (MKS Instruments).

HRTEM investigations (high resolution transmission electron microscopy) were performed to investigate the particle size and morphology of the catalysts. The samples were added to iso-propanol and the resulting dispersion was then put in an ultrasonic device, in which simultaneous break-up of agglomerates and coating of a silicium covered grid occurred. After drying at ambient conditions, HRTEM images were taken in bright field mode. A TEM EM912 from Omega/Carl-Zeiss was used providing a resolution of ca. 0.4 nm.

Thermogravimetry (TG) coupled with difference temperature analysis (DTA) was used for the examination of the thermal stability of the catalysts. The TG/DTA analyses were made on a STA 409 from Netzsch. A sample mass between 20 mg and 50 mg was taken and heated from 100 °C to 650 °C with a ramp of 3.3 K min<sup>−1</sup>, while adjusting a flow of 500 ml min<sup>−1</sup> of synthetic air (Air Liquide) dosed by a flow controller (Brooks Instruments).

$N_2$  physisorption was conducted with a Porotec Sorptomatic 1990. The respective sample was pre-treated at 250 °C for 15 min in a vacuum of 10<sup>−4</sup> mbar and cooled down to −196 °C. Then, the  $N_2$  isotherm was recorded. The BET surface area ( $S_{BET}$ ) was derived from the adsorption data taken at  $p/p_0$  ratios of 0.05–0.30. Total pore volume including interparticulate space was derived from the  $N_2$  volume physisorbed at  $p/p_0 = 0.99$ .

The soot was produced in a diffusion burner using a  $C_3H_6/O_2$  flame as reported recently [30]. Relevant physical-chemical characteristics of this soot are as follows: chemical composition: 97.5 wt.% C, 0.6 wt.% H, 0.2 wt.% N, 1.5 wt.% O, content of volatile matter: 4 wt.%, higher heating value: 33.35 MJ kg<sup>−1</sup>, BET surface area: 92 m<sup>2</sup> g<sup>−1</sup> [31]. These characteristics indicate that the  $C_3H_6$ -soot rather represents a diesel soot formed under full load conditions.

## 2.2. Catalytic studies

The activity of the iron oxide catalysts was investigated by TPO (temperature programmed oxidation) using a tight contact catalyst/soot mixture of 1.66 g (10 mmol  $\text{Fe}_2\text{O}_3$  and 5 mmol soot). The blend was packed in a quartz glass tube reactor (i.d. 10 mm) and fixed by quartz wool. Temperature was monitored by two K-type thermocouples located directly in front of and behind the fixed-bed. In TPO, the temperature was linearly increased at a rate of  $3.3 \text{ K min}^{-1}$ , while feeding a model exhaust of 10 vol.%  $\text{O}_2$  and 90 vol.%  $\text{N}_2$  (Air Liquide) supplied by two independent flow controllers (MKS Instruments). The total flow was  $500 \text{ ml min}^{-1}$  (STP) corresponding to a space velocity of  $15,000 \text{ h}^{-1}$ . CO and  $\text{CO}_2$  effluents were analysed by NDIR (BINOS 1.2, Leybold-Heraeus).

The mixture of catalyst and soot was prepared by ball milling (Pulverisette 0, Fritsch) for 15 min using a hardened steel ball ( $m = 940 \text{ g}$ ). Finally, the blend was pelletised and granulated as done for TPD. Former investigations demonstrated that the ball milling represents the crucial preparation step resulting in tight contact of catalyst and soot. This contact mode is close to a certain part of diesel soot deposited on a catalytic DPF [17,32].

## 3. Results and discussion

### 3.1. Physical–chemical characteristics of the catalysts

The analysis of the X-ray reflexes of the PVA- $\text{Fe}_2\text{O}_3$  sample (Fig. 1) indicates  $\alpha\text{-Fe}_2\text{O}_3$  to be the only crystalline phase

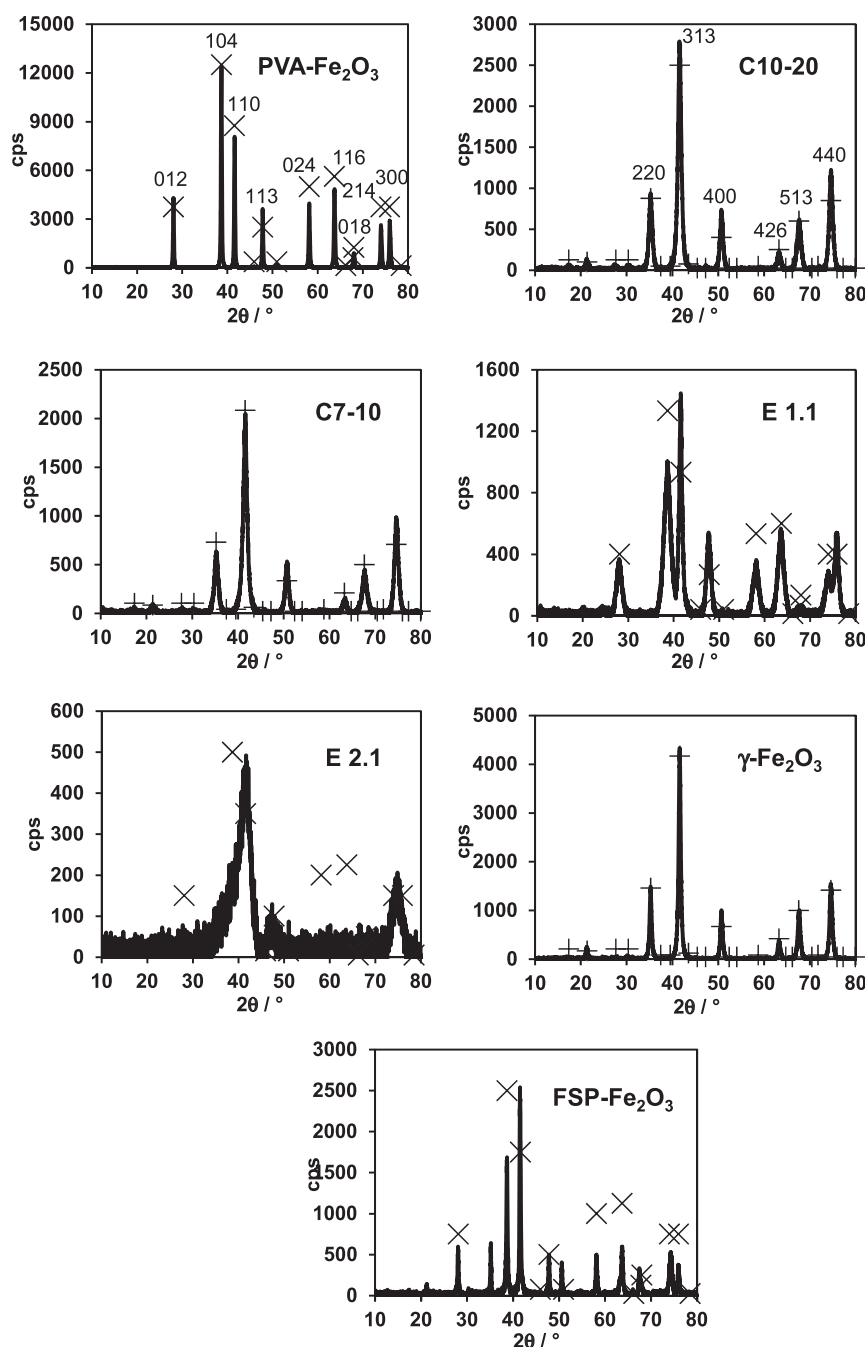
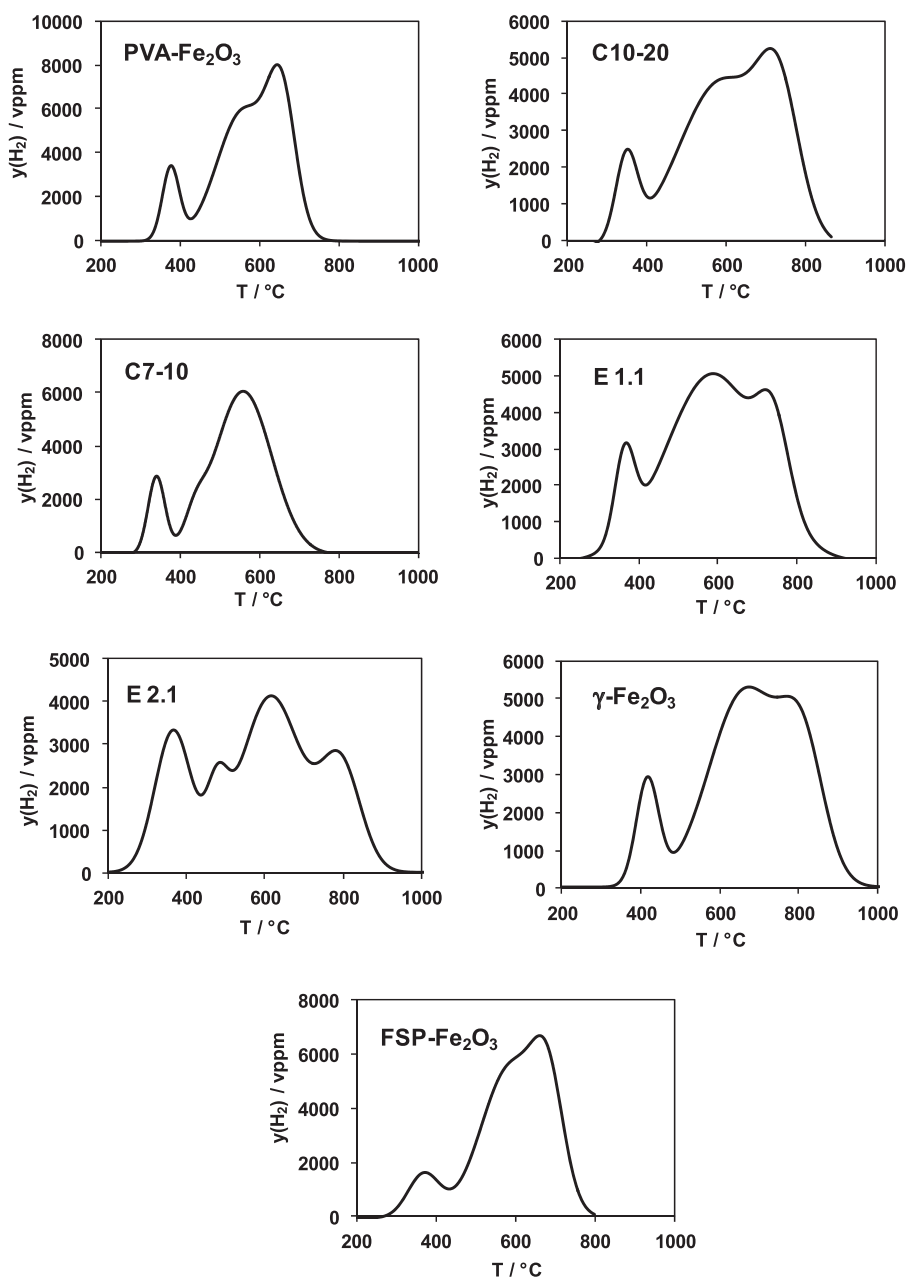


Fig. 1. PXRD patterns of the iron oxide samples. Theoretical line profiles of  $\alpha\text{-Fe}_2\text{O}_3$  (x) and  $\gamma\text{-Fe}_2\text{O}_3$  (+) are demonstrated for comparison.



**Fig. 2.** HTPR profiles of the iron oxide samples. Conditions:  $y(\text{H}_2) = 5 \text{ vol.}\%$ ,  $y(\text{Ar}) = 95 \text{ vol.}\%$ ,  $F = 200 \text{ ml min}^{-1}$ ,  $\beta = 15 \text{ K min}^{-1}$ ,  $m = 60 \text{ mg}$ .

without any significant amorphous domains. The HTPR profile (Fig. 2) is also typical for  $\alpha\text{-Fe}_2\text{O}_3$  implying the reduction sequence  $\text{Fe}_2\text{O}_3 \rightarrow \text{Fe}_3\text{O}_4$  at low temperature (ca.  $380^\circ\text{C}$ ) and  $\text{Fe}_3\text{O}_4 \rightarrow \text{FeO} \rightarrow \text{Fe}$  at higher temperature (ca.  $650^\circ\text{C}$ ). The ratio of high to low temperature  $\text{H}_2$  conversion amounts to 8, while the total molar ratio of consumed  $\text{H}_2$  to Fe is 1.5 [33].

From the Rietveld refinement of the diffractogram of C10-20 (Fig. 1) a crystalline proportion of about 90% is obtained with a proportion of ca. 63%  $\gamma\text{-Fe}_2\text{O}_3$  and ca. 27%  $\text{Fe}_3\text{O}_4$ . But, it has to be mentioned that  $\gamma\text{-Fe}_2\text{O}_3$  and  $\text{Fe}_3\text{O}_4$  reveal a very similar structure due to the face-centered cubic unit cell of the oxygen anions and the occupation of tetrahedral and octahedral sites by the iron cations. Thus, the result of the Rietveld refinement has to be taken with care. However, the existence of  $\text{Fe}^{2+}$  species is confirmed by HTPR evidencing a ratio of high- to low-temperature  $\text{H}_2$  consumption of about 10 and a molar  $\text{H}_2/\text{Fe}$  ratio of approx. 1.3 (Fig. 2). The later suggests the existence of amorphous domains in the form of

$\text{FeO}$  or  $\text{Fe}_3\text{O}_4$ , which imply a total  $\text{H}_2/\text{Fe}$  proportion of 1.0 and 1.3. However,  $\text{FeO}$  is unstable under atmospheric conditions [25] and therefore the HTPR data are interpreted to confirm the presence of  $\text{Fe}_3\text{O}_4$  as shown by PXRD. Also, it is known that  $\text{Fe}_3\text{O}_4$  and  $\gamma\text{-Fe}_2\text{O}_3$  often coexist as solid solution [25,27]. C7-10 reveals a PXRD pattern (Fig. 1) comprising a crystalline fraction of ca. 90% with an estimated fraction of 62%  $\gamma\text{-Fe}_2\text{O}_3$  and 38%  $\text{Fe}_3\text{O}_4$ . The presence of  $\text{Fe}^{2+}$  cations is also demonstrated by HTPR, which features a high to low temperature  $\text{H}_2$  consumption of ca. 7.5 and a  $\text{H}_2/\text{Fe}$  ratio of ca. 1.1 (Fig. 2).

From the X-ray diffractogram of E 1.1 (Fig. 1) a crystalline proportion of ca. 90% with a single contribution of  $\alpha\text{-Fe}_2\text{O}_3$  is derived. The HTPR profile confirms the major content of  $\alpha\text{-Fe}_2\text{O}_3$ , whereas the  $\text{H}_2/\text{Fe}$  ratio of ca. 1.4 indicates major appearance of  $\text{Fe}^{3+}$  (Fig. 2). The PXRD pattern of E 2.1 shows three weak and relatively broad reflexes (Fig. 1), which tentatively refer to  $\alpha\text{-Fe}_2\text{O}_3$ , but obviously the sample is predominately amorphous. Also, the HTPR trace is complex and cannot be attributed to the typical reduction sequence



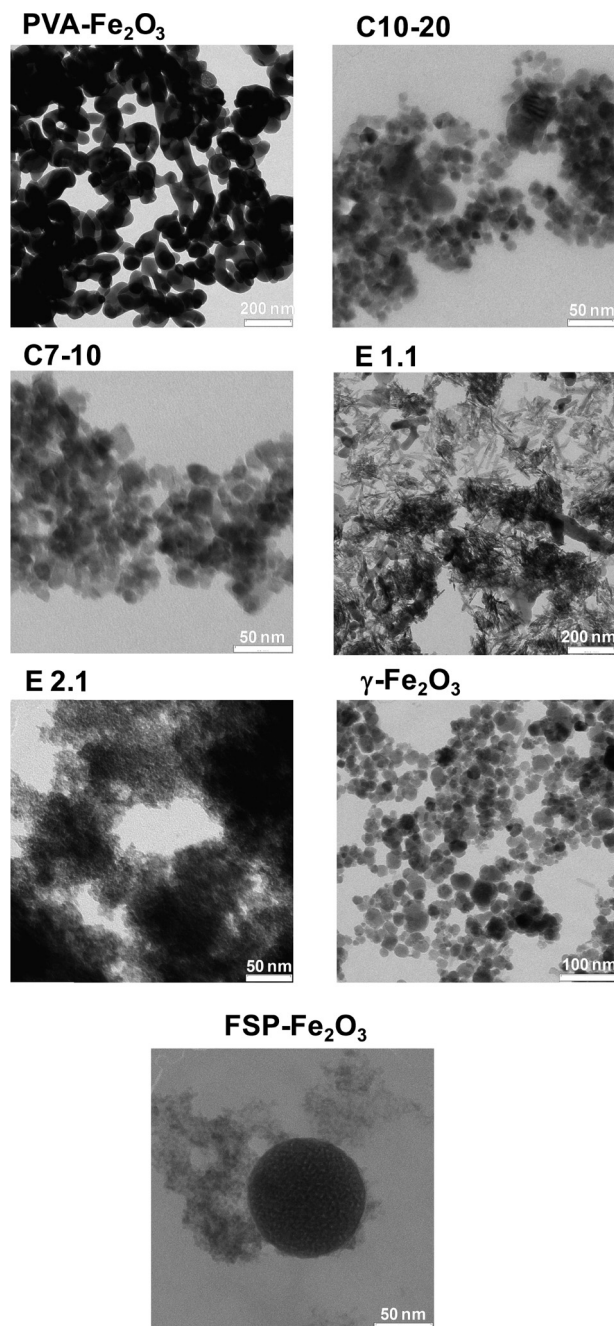


Fig. 3. Bright field HRTEM images of the iron oxide samples.

of  $\alpha$ -Fe<sub>2</sub>O<sub>3</sub> and Fe<sub>3</sub>O<sub>4</sub>, respectively (Fig. 2). From the total H<sub>2</sub>/Fe ratio of about 1.4 a minor content of Fe<sup>2+</sup> is deduced.

The phase analysis of the  $\gamma$ -Fe<sub>2</sub>O<sub>3</sub> sample (Fig. 1) indicates a crystallinity of about 80%. Since the HTPR profile closely resembles that of  $\alpha$ -Fe<sub>2</sub>O<sub>3</sub>, i.e. the ratio of high- to low-temperature H<sub>2</sub> consumption is about 8 and the H<sub>2</sub>/Fe ratio is close to 1.5 (Fig. 2). Hence,  $\gamma$ -Fe<sub>2</sub>O<sub>3</sub> is supposed to be the major phase.

The PXRD analysis of FSP-Fe<sub>2</sub>O<sub>3</sub> (Fig. 1) provides a crystalline fraction of 50% including 66%  $\alpha$ -Fe<sub>2</sub>O<sub>3</sub>, 19%  $\gamma$ -Fe<sub>2</sub>O<sub>3</sub> and 15% Fe<sub>3</sub>O<sub>4</sub>. The HTPR profile (Fig. 2) is rather typical for Fe<sub>2</sub>O<sub>3</sub> with high to low temperature H<sub>2</sub> conversion of 8.7, whereas the total H<sub>2</sub>/Fe ratio of ca. 1.3 suggests the presence of Fe<sup>2+</sup> cations as well.

The HRTEM images of the catalysts are shown in Fig. 3. The PVA-Fe<sub>2</sub>O<sub>3</sub> particles range from 80 to 200 nm, whereas C10–20 reveals primary particles between 10 nm and 20 nm as well as large agglomerates. Moreover, C7–10 mainly exhibits particles between

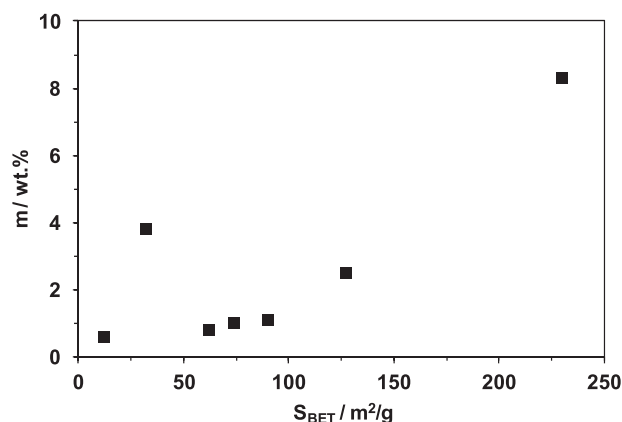


Fig. 4. TG mass loss in dependency of the BET surface area of the iron oxide samples.

7 nm and 10 nm. Contrary, E 1.1 contains a multiplicity of particle shapes and sizes. The major part is specular and has a length from 50 nm to 100 nm at a diameter of 2–5 nm. Also, spherical particles are observed with diameters of more than 200 nm. The HRTEM images of  $\gamma$ -Fe<sub>2</sub>O<sub>3</sub> show particle sizes within a range from 10 nm to 100 nm, while FSP-Fe<sub>2</sub>O<sub>3</sub> exhibits primary particles with a mean diameter of ca. 5 nm and spherical agglomerates with a diameter of ca. 100 nm.

The BET surface area as well as the pore volume of the iron oxide catalysts are demonstrated in Table 1 showing big differences in BET surface area (13–230 m<sup>2</sup> g<sup>−1</sup>), but rather similar pore volumes ranging from ca. 0.15 to 0.53 ml g<sup>−1</sup>. Furthermore, the TG-DTA analyses of the samples demonstrate a clear increase in mass loss with BET surface area. However, FSP-Fe<sub>2</sub>O<sub>3</sub> represents an exception, which reveals a relatively high mass loss of ca. 3.8 wt.% at a BET surface area of about 32 m<sup>2</sup> g<sup>−1</sup> (Fig. 4). The decrease in mass is always combined with endothermic DTA signal and is therefore attributed to disappearance of water due to desorption and dehydroxylation occurring on the surface. This strong decline of the FSP-Fe<sub>2</sub>O<sub>3</sub> mass is likely related to hydrocarbons and NO<sub>x</sub> species originated from the flame spray synthesis. The presence of these components was proven through diffuse reflectance infrared spectroscopy. As a result of the TG/DTA investigations, all the catalysts are stable under oxygen-rich conditions up to temperatures of 650 °C.

Moreover, the O<sub>2</sub>-TPD studies performed up to 700 °C provide no O<sub>2</sub> desorption above the limit of the CIMS detector (5 ppm), although masses up to 5 g were taken. Thus, O<sub>2</sub>-TPD suggests that the iron oxides tested do not show any oxygen storage capacity under conditions relevant for the catalytic measurements.

### 3.2. Kinetic modelling of the NH<sub>3</sub> adsorption and desorption

The NH<sub>3</sub>-TPD data were used for modelling the adsorption and desorption of NH<sub>3</sub> on the iron oxides. This kinetic model differentiates Bronsted and Lewis acid sites and it therefore comprises two sets of kinetic parameters providing the respective quantity of acid sites. The NH<sub>3</sub> adsorption and desorption on Bronsted acid sites implies the formation and decomposition of NH<sub>4</sub><sup>+</sup> species originated from the interaction of NH<sub>3</sub> with surface hydroxide groups [34,35] denoted as H<sup>+</sup> (Eq. (1)). The adsorption and desorption of NH<sub>3</sub> on Lewis acid Fe<sup>3+</sup> site (\*) is described by Eq. (2) [35].



**Table 1**

Physical–chemical characteristics of the iron oxide samples.

	PVA-Fe <sub>2</sub> O <sub>3</sub>	C10-20	C7-10	E 1.1	E 2.1	γ-Fe <sub>2</sub> O <sub>3</sub>	FSP-Fe <sub>2</sub> O <sub>3</sub>
T <sub>CO<sub>2</sub>,max</sub> /°C	408	388	376	368	414	381	332
Cryst./%	100	90	90	86	0	80	50
S <sub>BET</sub> /m <sup>2</sup> g <sup>-1</sup>	12	74	90	127	230	62	32
V <sub>pore</sub> /cm <sup>3</sup> /g	0.15	0.26	0.28	0.54	0.41	0.41	0.16
Γ <sub>NH<sub>4</sub><sup>+</sup></sub> /μmol/m <sup>2</sup>	0.90	0.84	3.00	1.20	0.67	0.70	1.30
Γ <sub>NH<sub>3</sub></sub> /μmol/m <sup>2</sup>	0.70	0.03	0.12	0.60	0.64	0.90	1.40
d <sub>particle</sub> /nm	80–200	10–20	7–10	5 × 50	1–5	10–100	5–100

The kinetic model includes the mean field approximation considering all Bronsted and Lewis acid sites to be equivalent. This assumption is generally used as an effective standard method in the modelling of heterogeneous surface reactions [34,35]. The reaction rates are expressed by an Arrhenius-based approach (Eqs. (3)–(6));  $A_i$  is the pre-exponential factor,  $E_i$  the activation energy,  $c(i)$  the respective gas phase concentration,  $\Theta_{\text{Fe}^{3+}}$  and  $\Theta_{\text{H}^+}$  are the specific fractions of free adsorption sites. For the desorption of NH<sub>3</sub>, a linear decrease in activation energy with rising coverage is supposed due to repulsion of adsorbed species [36]. Thus, for determination of the activation energy of desorption the activation energy at zero coverage ( $E_i(0)$ ) is correlated with the coverage by introducing the factor  $\alpha_i$  (Eqs. (4) and (6)).  $\Theta_{\text{NH}_4^+}$  and  $\Theta_{\text{NH}_3}$  are the coverages by NH<sub>4</sub><sup>+</sup> and NH<sub>3</sub> defined as  $\Theta_i = n_i/(\Gamma_i S)$ ;  $n_i$  is the molar quantity of adsorbed amount of species  $i$ ,  $\Gamma_i$  the surface concentration of free sites and  $S$  is the absolute surface area.

$$r_1 = A_1 \cdot \exp\left(-\frac{E_1}{RT}\right) \cdot c(\text{NH}_3) \cdot \Theta_{\text{H}^+} \quad (3)$$

$$r_2 = A_2 \cdot \exp\left(-\frac{E_2(0) - \alpha_2 \Theta_{\text{NH}_4^+}}{RT}\right) \cdot \Theta_{\text{NH}_4^+} \quad (4)$$

$$r_3 = A_3 \cdot \exp\left(-\frac{E_3}{RT}\right) \cdot c(\text{NH}_3) \cdot \Theta_{\text{Fe}^{3+}} \quad (5)$$

$$r_4 = A_4 \cdot \exp\left(-\frac{E_4(0) - \alpha_4 \Theta_{\text{NH}_3}}{RT}\right) \cdot \Theta_{\text{NH}_3} \quad (6)$$

The modelling of the NH<sub>3</sub>-TPD is based upon the mass balance of gaseous NH<sub>3</sub> as well as NH<sub>3</sub> and NH<sub>4</sub><sup>+</sup> surface species (Eqs. (7)–(9)) leading to a system of an algebraic and two non-linear differential equations;  $F$  is the total gas flow and  $\beta$  the heating rate. The employed tube reactor is described by the model of a stationary CSTR being in fair agreement with literature on TPD modelling [34,37].

$$F \cdot c(\text{NH}_3)_{\text{out}} = F \cdot c(\text{NH}_3)_{\text{in}} - S \cdot r_1 + S \cdot r_2 - S \cdot r_3 + S \cdot r_4 \quad (7)$$

$$S \cdot \Gamma_{\text{NH}_4^+} \beta \frac{d\Theta_{\text{NH}_4^+}}{dT} = S \cdot r_1 - S \cdot r_2 \quad (8)$$

$$S \cdot \Gamma_{\text{NH}_3} \beta \frac{d\Theta_{\text{NH}_3}}{dT} = S \cdot r_3 - S \cdot r_4 \quad (9)$$

To reduce the number of free parameters within the fitting procedure, the pre-exponential factors of adsorption were calculated by using Eq. (10) derived from the kinetic gas theory;  $N_A$  is the Avogadro number,  $a_m$  the required space of an NH<sub>3</sub> molecule and  $S^0$  the sticking coefficient. Due to the lack of literature data the sticking coefficient of NH<sub>3</sub> on the (1 1 0) plane of Fe ( $S^0 = 0.10$ ) was used for the calculation of the pre-exponential factor  $A_i$  of NH<sub>3</sub> on Lewis as well as Bronsted acid sites for all the samples [35].  $a_m$  was

calculated to be  $2 \cdot 10^{-20} \text{ m}^2$  as deduced from the cross section area of NH<sub>3</sub> ( $d = 1.6 \text{ \AA}$ ).

$$A_i = \frac{N_A RT}{(2\pi M_i RT)^{1/2}} a_m \Gamma_i S^0 \quad (10)$$

For calculation of the surface concentrations  $\Gamma_{\text{NH}_4^+}$  and  $\Gamma_{\text{NH}_3}$ , the desorbed amount of Lewis and Bronsted bond NH<sub>3</sub> was derived from the de-convoluted TPD spectrum, i.e.  $\Gamma_i = n_{i,\text{full}}/S$  with  $n_{i,\text{full}} = \left(10^{-4} \frac{1}{V_m} F \frac{1}{\beta} \int_T^{T_{\text{max}}} y(\text{NH}_3) dT\right) \cdot n_{\text{NH}_3,\text{full}}$  and  $n_{\text{NH}_4^+,\text{full}}$  were estimated by deconvoluting the NH<sub>3</sub>-TPD traces using Gaussian function [35]. The NH<sub>3</sub>-TPD feature found at lower temperatures (ca. 135 °C) refers to the decomposition of NH<sub>4</sub><sup>+</sup>, while that appearing at higher temperatures (approx. 250 °C) is ascribed to the desorption of NH<sub>3</sub> from Lewis acid sites (Fig. 5) [34,35].

Furthermore, the activation energy for adsorption is neglected ( $E_2 = E_4 = 0 \text{ kJ mol}^{-1}$ ) being in line with literature [35]. It should be mentioned that the model assumes complete surface coverage at the beginning of every TPD. The surface coverage was calculated by using the Matlab tool ode15s, while the free parameters  $A_2$ ,  $E_2(0)$ ,  $\alpha_2$ ,  $A_4$ ,  $E_4(0)$  and  $\alpha_4$ , were estimated with lsqcurvefit. The reliability of the estimated parameters was assessed with the 95% confidence interval calculated by the Matlab function nlparci.

The results of the calculations are presented in Fig. 5 showing that the TPD curves obtained after NH<sub>3</sub> exposure at 50 °C are satisfactorily reproduced by the kinetic model and the parameters implemented therein. For model validation, the TPD patterns after NH<sub>3</sub> treatment at 150 °C were predicted using the kinetic model. The comparison with the experimental traces shows good agreement (Fig. 5) thus substantiating the model. The kinetic parameters are listed in Table 2 indicating for all samples very similar values of the NH<sub>3</sub> adsorption/desorption on the Bronsted and Lewis acid sites, respectively.

The activation energy of the Bronsted bond NH<sub>3</sub> species ranges from 100 to 112 kJ mol<sup>-1</sup>, the pre-exponential factors of NH<sub>4</sub><sup>+</sup> decomposition are in the order of  $10^{10} \text{ mol s}^{-1} \text{ m}^{-2}$  and the  $\alpha_2$  factors lie between 3 and 22 kJ mol<sup>-1</sup>. The kinetic parameters of molecularly sorbing NH<sub>3</sub> vary for  $E_4$  between 120 and 133 kJ mol<sup>-1</sup>, for  $A_4$  between  $9 \times 10^8$  and  $5.5 \times 10^{10} \text{ mol s}^{-1} \text{ m}^{-2}$  and for  $\alpha_4$  between 3 and 22 kJ mol<sup>-1</sup>. The comparison with the Bronsted acid sites of ZrO<sub>2</sub> samples shows a range of  $E_2(0)$  from 100 to 105 kJ mol<sup>-1</sup> [34], while  $E_2(0)$  of Fe/HBEA zeolite (Si/Al = 12.5) lies between 110 and 128 kJ mol<sup>-1</sup> [35]. For the Lewis acid sites of ZrO<sub>2</sub> and Fe/HBEA,  $E_4(0)$  ranges from 141 and 163 kJ mol<sup>-1</sup> and from 140 to 157 kJ mol<sup>-1</sup>, respectively. These reference data show that the determined activation energies for the release of the NH<sub>3</sub> and NH<sub>4</sub><sup>+</sup> surface species are very close to that of related materials.

### 3.3. Results of the TPO studies

The TPO profiles of all catalysts show CO<sub>2</sub> formation in a relatively small temperature regime of about 30 K characterised by a clear CO<sub>2</sub> peak. The amount of CO<sub>2</sub> indicates complete soot consumption upon the experiments. In contrast to TPO study performed without catalyst, carbon monoxide is not found in the

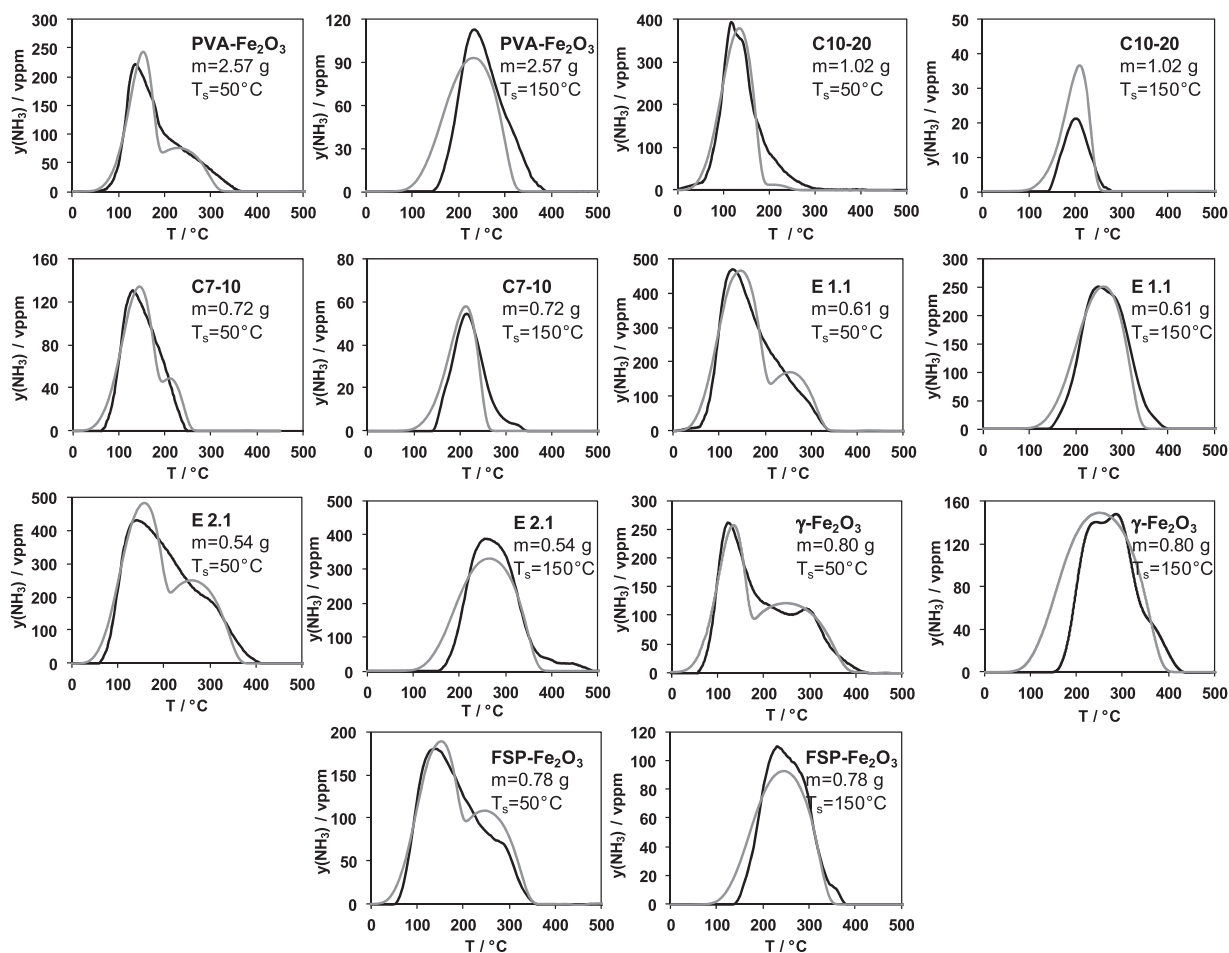


**Fig. 5.** Experimental (—) and calculated (---)  $\text{NH}_3$ -TPD profiles of the iron oxide samples obtained after saturation at a temperature ( $T_s$ ) of 50 and 150 °C. Conditions:  $F(\text{N}_2) = 500 \text{ ml min}^{-1}$  (STP),  $\beta = 10 \text{ K min}^{-1}$ , mass of respective sample is given in the figure.

presence of the catalysts due to their CO oxidation activity [17,19]. For the assessment of the soot oxidation performance of the iron oxides, the temperature of maximum  $\text{CO}_2$  production ( $T_{\text{CO}_2, \text{max}}$ ) is taken indicating highest activity for FSP- $\text{Fe}_2\text{O}_3$  ( $T_{\text{CO}_2, \text{max}} = 332^\circ\text{C}$ ) and lowest efficiency for E 2.1 ( $T_{\text{CO}_2, \text{max}} = 414^\circ\text{C}$ ); the reproducibility of  $T_{\text{CO}_2, \text{max}}$  is in the range of  $\pm 10 \text{ K}$ . For clarity, the TPO profile of the FSP- $\text{Fe}_2\text{O}_3$  catalyst is shown in Fig. 6, whereas all  $T_{\text{CO}_2, \text{max}}$  values are summarised in Table 1. For reference purposes, it should be stated that in TPO with bare soot  $T_{\text{CO}_2, \text{max}}$  is found at  $570^\circ\text{C}$  clearly demonstrating the effect of the catalysts [19].

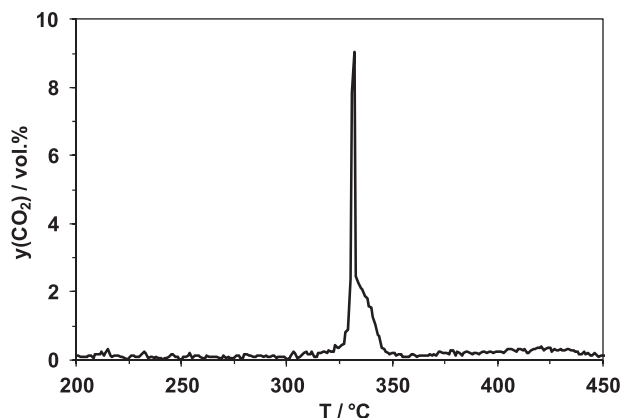


**Fig. 6.** TPO profile of the FSP- $\text{Fe}_2\text{O}_3$ /soot mixture. Conditions:  $y(\text{O}_2) = 10 \text{ vol.}\%$ ,  $y(\text{N}_2) = 90 \text{ vol.}\%$ ,  $F = 500 \text{ ml min}^{-1}$  (STP),  $\beta = 1.8 \text{ K min}^{-1}$ ,  $m(\text{mixture}) = 1.66 \text{ g}$ ,  $n(\text{Fe}_2\text{O}_3) = 10 \text{ mmol}$ ,  $n(\text{soot}) = 5 \text{ mmol}$ , tight contact mode.

### 3.4. Coupling of physical–chemical properties and activity of the iron oxide catalysts

In this section, the correlation of the soot oxidation activity and determining physical–chemical characteristics of the fresh iron oxide catalysts is evaluated. As a result, a connection between catalytic activity and number of Bronsted sites, BET surface area, total pore volume and particle size as well as HTPR features, i.e. temperature of low temperature peak, ratio of high to low temperature  $\text{H}_2$  consumption and proportion of  $\text{H}_2/\text{Fe}$ , cannot be deduced. However, Fig. 7 (left) basically suggests a trend of increasing activity expressed as decreasing  $T_{\text{CO}_2, \text{max}}$  with proportion of Lewis acid sites. However, it should be stated that a clear dependency of soot oxidation activity is only observed for rather higher surface concentrations of Lewis acid sites, i.e. above ca.  $0.6 \mu\text{mol m}^{-2}$ . Furthermore, a correlation of relative crystallinity and activity is found as well. Fig. 7 (right) shows that starting from a crystalline fraction of 1 decreasing crystalline order firstly increases the catalytic activity as indicated by declining  $T_{\text{CO}_2, \text{max}}$ , but for a crystalline proportion of about 0  $T_{\text{CO}_2, \text{max}}$  is similar to that of highly crystallised samples, i.e. the activity is clearly decreased as referred to a middle crystallinity.

The effect of Lewis acid sites and crystallinity shows that a balance of both features seems to be important for high soot activity in soot oxidation. The relationship between Lewis acid sites, crystalline proportion and catalytic activity is expressed by Fig. 8. This contour diagram demonstrates highest activity for moderate crystallinity (ca. 0.5) and a high amount of specific Lewis acid sites, whereas a moderate quantity of specific Lewis bond  $\text{NH}_3$  and high

**Table 2**  
Kinetic parameters of NH<sub>3</sub> adsorption/desorption on the iron oxide samples.

Sample	Parameter	Value	Tolerance	Unit	Reference
FSP-Fe <sub>2</sub> O <sub>3</sub>	A <sub>1</sub> , A <sub>3</sub>	0.30		m s <sup>-1</sup>	Calculated
	E <sub>1</sub> , E <sub>3</sub>	0		kJ mol <sup>-1</sup>	
	A <sub>2</sub>	1.0 × 10 <sup>10</sup>	4.3 × 10 <sup>-2</sup>	mol sm <sup>-2</sup>	Fit
	E <sub>2</sub>	105	1.3 × 10 <sup>-5</sup>	kJ mol <sup>-1</sup>	Fit
	α <sub>2</sub>	10	1.1 × 10 <sup>-6</sup>	kJ mol <sup>-1</sup>	Fit
	A <sub>4</sub>	1.0 10 <sup>9</sup>	3.8 × 10 <sup>1</sup>	mol sm <sup>-2</sup>	Fit
	E <sub>4</sub>	128	1.9 × 10 <sup>-2</sup>	kJ mol <sup>-1</sup>	Fit
	α <sub>4</sub>	18	1.9 × 10 <sup>-2</sup>	kJ mol <sup>-1</sup>	Fit
C10-20	A <sub>1</sub> , A <sub>3</sub>	0.3		m s <sup>-1</sup>	Calculated
	E <sub>1</sub> , E <sub>3</sub>	0		kJ mol <sup>-1</sup>	
	A <sub>2</sub>	4.4 × 10 <sup>10</sup>	2.8 × 10 <sup>-2</sup>	mol sm <sup>-2</sup>	Fit
	E <sub>2</sub>	104	8.8 × 10 <sup>-7</sup>	kJ mol <sup>-1</sup>	Fit
	α <sub>2</sub>	7	1.1 × 10 <sup>-7</sup>	kJ mol <sup>-1</sup>	Fit
	A <sub>4</sub>	1.0 × 10 <sup>9</sup>	9.2	mol sm <sup>-2</sup>	Fit
	E <sub>4</sub>	120	5.5 × 10 <sup>-5</sup>	kJ mol <sup>-1</sup>	Fit
	α <sub>4</sub>	5.2	4.6 × 10 <sup>-6</sup>	kJ mol <sup>-1</sup>	Fit
C7-10	A <sub>1</sub> , A <sub>3</sub>	0.3		m s <sup>-1</sup>	Calculated
	E <sub>1</sub> , E <sub>3</sub>	0		kJ mol <sup>-1</sup>	
	A <sub>2</sub>	1.5 × 10 <sup>10</sup>	5.7 × 10 <sup>-2</sup>	mol sm <sup>-2</sup>	Fit
	E <sub>2</sub>	105	9.7 × 10 <sup>-7</sup>	kJ mol <sup>-1</sup>	Fit
	α <sub>2</sub>	5.7	3.2 × 10 <sup>-8</sup>	kJ mol <sup>-1</sup>	Fit
	A <sub>4</sub>	5.5 × 10 <sup>10</sup>	1.71	mol sm <sup>-2</sup>	Fit
	E <sub>4</sub>	121	1.4 × 10 <sup>-5</sup>	kJ mol <sup>-1</sup>	Fit
	α <sub>4</sub>	3	4.1 × 10 <sup>-7</sup>	kJ mol <sup>-1</sup>	Fit
E 1.1	A <sub>1</sub> , A <sub>3</sub>	0.3		m s <sup>-1</sup>	Calculated
	E <sub>1</sub> , E <sub>3</sub>	0		kJ mol <sup>-1</sup>	
	A <sub>2</sub>	3.0 × e <sup>10</sup>	0.15	mol sm <sup>-2</sup>	Fit
	E <sub>2</sub>	106	1.5 × 10 <sup>-6</sup>	kJ mol <sup>-1</sup>	Fit
	α <sub>2</sub>	10.9	5.8 × 10 <sup>-7</sup>	kJ mol <sup>-1</sup>	Fit
	A <sub>4</sub>	4.0 × 10 <sup>9</sup>	9.1	mol sm <sup>-2</sup>	Fit
	E <sub>4</sub>	130	1.6 × 10 <sup>-4</sup>	kJ mol <sup>-1</sup>	Fit
	α <sub>4</sub>	12	3.5 × 10 <sup>-6</sup>	kJ mol <sup>-1</sup>	Fit
E 2.1	A <sub>1</sub> , A <sub>3</sub>	0.30		m s <sup>-1</sup>	Calculated
	E <sub>1</sub> , E <sub>3</sub>	0		kJ mol <sup>-1</sup>	
	A <sub>2</sub>	8.0 10 <sup>10</sup>	1.23 × 10 <sup>-1</sup>	mol sm <sup>-2</sup>	Fit
	E <sub>2</sub>	112	3.1 × 10 <sup>-6</sup>	kJ mol <sup>-1</sup>	Fit
	α <sub>2</sub>	14	3.1 × 10 <sup>-7</sup>	kJ mol <sup>-1</sup>	Fit
	A <sub>4</sub>	3.0 10 <sup>9</sup>	7.9	mol sm <sup>-2</sup>	Fit
	E <sub>4</sub>	133	5.7 × 10 <sup>-4</sup>	kJ mol <sup>-1</sup>	Fit
	α <sub>4</sub>	19	2.6 × 10 <sup>-4</sup>	kJ mol <sup>-1</sup>	Fit
PVA-Fe <sub>2</sub> O <sub>3</sub>	A <sub>1</sub> , A <sub>3</sub>	0.3		m s <sup>-1</sup>	Calculated
	E <sub>1</sub> , E <sub>3</sub>	0		kJ mol <sup>-1</sup>	
	A <sub>2</sub>	9.0 × 10 <sup>10</sup>	4.2 × 10 <sup>-2</sup>	mol sm <sup>-2</sup>	Fit
	E <sub>2</sub>	110	1.8 × 10 <sup>-7</sup>	kJ mol <sup>-1</sup>	Fit
	α <sub>2</sub>	2	1 × 10 <sup>-8</sup>	kJ mol <sup>-1</sup>	Fit
	A <sub>4</sub>	9.0 × 10 <sup>8</sup>	1.0 × 10 <sup>1</sup>	mol sm <sup>-2</sup>	Fit
	E <sub>4</sub>	123	2.1 × 10 <sup>-4</sup>	kJ mol <sup>-1</sup>	Fit
	α <sub>4</sub>	15	4.9 × 10 <sup>-5</sup>	kJ mol <sup>-1</sup>	Fit
γ-Fe <sub>2</sub> O <sub>3</sub>	A <sub>1</sub> , A <sub>3</sub>	0.3		m s <sup>-1</sup>	Calculated
	E <sub>1</sub> , E <sub>3</sub>	0		kJ mol <sup>-1</sup>	
	A <sub>2</sub>	5.0 × 10 <sup>10</sup>	8.0 × 10 <sup>-2</sup>	mol sm <sup>-2</sup>	Fit
	E <sub>2</sub>	100	1.6 × 10 <sup>-5</sup>	kJ mol <sup>-1</sup>	Fit
	α <sub>2</sub>	4	3.8 × 10 <sup>-8</sup>	kJ mol <sup>-1</sup>	Fit
	A <sub>4</sub>	1.0 × 10 <sup>8</sup>	2.1 × 10 <sup>1</sup>	mol sm <sup>-2</sup>	Fit
	E <sub>4</sub>	116	2.0 × 10 <sup>-4</sup>	kJ mol <sup>-1</sup>	Fit
	α <sub>4</sub>	22	6.5 × 10 <sup>-5</sup>	kJ mol <sup>-1</sup>	Fit

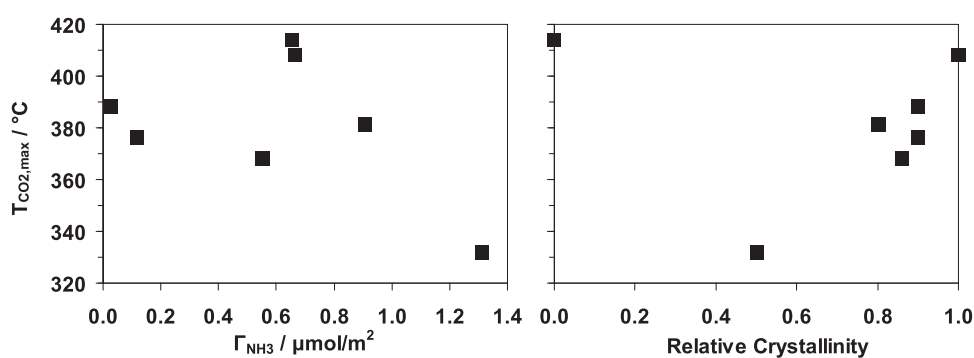


**Fig. 7.**  $T_{\text{CO}_2, \text{max}}$  upon catalytic TPO in dependency of the surface concentration of Lewis acid sites (left) and the relative crystallinity (right) of the iron oxide samples.



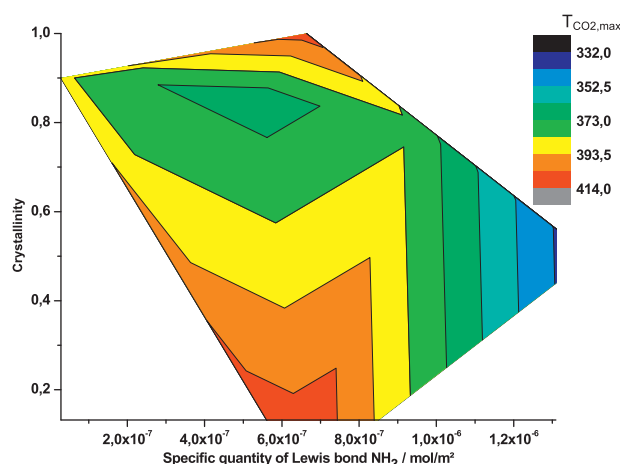


Fig. 8. Contour plot of the correlation between  $T_{\text{CO}_2,\text{max}}$ , quantity of specific Lewis bond  $\text{NH}_3$  and crystallinity of the iron oxide catalysts.

(1.0) or low (ca. 0) crystallinity reveal poor activity. The importance of Lewis acid surface sites is ascribed to their capability of transferring oxygen [19,38], whereas the  $\text{NH}_3$  adsorption/desorption model constructed in this paper points to very similar nature of these surface sites for all iron oxides investigated. Moreover, our mechanistic studies with  $^{18}\text{O}_2$  reported lately [19] suggest that oxygen is pumped from the iron oxide to the soot by physical contact points thus leaving oxygen vacancies on the catalyst surface, i.e. Lewis acid sites. These vacancies are refilled by diffusion of surface and bulk oxygen. In surface diffusion, oxygen migrates from neighbouring Lewis acid sites thus producing a cascade of formation and refilling of surface defect sites. Contrary, diffusion of bulk oxygen occurs along lattice vacancies. In accordance with our recent isotopic examinations it is known from the literature that surface diffusion of oxygen is much faster than its bulk diffusion [19,39] and therefore the former transport mechanism provides the major contribution in soot oxidation on iron oxide. Nevertheless, the present structure–activity study also confirms the importance of the transport of crystalline oxygen, as the amorphous sample E 2.1 shows rather low catalytic activity, although it exhibits a medium surface concentration of Lewis acid sites. This finding is in line with literature indicating faster oxygen diffusion in crystalline structures as referred to amorphous domains [40]. Hence, the derived correlation between Lewis acid sites, crystallinity and catalytic activity coincides with the above stated mechanistic suggestions thus accounting for the highest efficiency of the FSP- $\text{Fe}_2\text{O}_3$  sample. This catalyst implies the largest number of surface defect sites as well as moderate crystallinity both evoking fast diffusion of oxygen to contact points.

#### 4. Conclusions

The objective of this paper was to unravel the relationship between physical–chemical characteristics and soot oxidation activity of iron oxides catalysts. Thus, a series of different iron oxide samples was selected and thoroughly screened. The results evidence moderate crystallinity and high amount of Lewis surface sites to be crucial for the oxidation of soot. These findings coincide with former mechanistic investigations implying the oxygen supply from gas phase and bulk of iron oxide via its surface to contact points of soot particles. Thus, amorphous domains rather promote diffusion of surface oxygen, whereas crystalline domains provide bulk oxygen transport. The resulting oxygen deficiency of the crystalline lattice is finally balanced by counterdiffusion of oxygen from the surface layer to the bulk. The knowledge on these determining

characteristics identified in this paper is considered to be an important tool for the targeted development of advanced iron oxide based catalysts for soot oxidation.

#### Acknowledgements

The authors thankfully acknowledge the cooperation and financial support of Umicore (Hanau). The supply of iron oxide materials from Lanxess is also acknowledged with gratitude.

#### References

- [1] M. Knaapen, P.J.A. Borm, C. Albrecht, R.P.F. Schins, *International Journal of Cancer* 109 (2004) 799.
- [2] M.Z. Jacobsen, *Nature* 409 (2001) 695.
- [3] O. Deutschmann, A.G. Konstantopoulos, in: *Catalytic Technology for Soot and Gaseous Pollution Control*, Wiley-VCH, Weinheim, 2010.
- [4] A. Setiabudi, M. Makkee, J.A. Moulijn, *Applied Catalysis B: Environmental* 50 (2004) 185.
- [5] P. Zelenka, W. Cartellieri, P. Duke, *Applied Catalysis B: Environmental* 7 (1996) 3.
- [6] O. Salvat, P. Marez, G. Belot, *SAE Technical Paper Series* 2000-01-0473.
- [7] B.A.A.L.v. Setten, J.M. Schouten, M. Makkee, J.A. Moulijn, *Applied Catalysis B: Environmental* 28 (2000) 253.
- [8] N. Guilhaume, B. Bassou, G. Bergeret, D. Bianchi, F. Bosselet, A. Desmartin-Chomel, B. Jouquet, C. Mirodatos, *Applied Catalysis B: Environmental* 119–120 (2012) 287.
- [9] S. Li, R. Kato, Q. Wang, T. Yamanaka, T. Takeguchi, W. Ueda, *Applied Catalysis B: Environmental* 93 (2010) 383.
- [10] Z. Li, M. Meng, Y. Zha, F. Dai, T. Hu, Y. Xie, J. Zhang, *Applied Catalysis B: Environmental* 65 (2012) 121–122.
- [11] E.C. Aneggi, d. Leitenburg, G. Dolcetti, A. Trovarelli, *Catalysis Today* 114 (2006) 40.
- [12] P. Doggali, H. Kusaba, S. Rayalu, Y. Teraoka, N. Labhsetwar, *Topics in Catalysis* 56 (2013) 457.
- [13] K. Krishna, A. Bueno-López, M. Makkee, J.A. Moulijn, *Applied Catalysis B: Environmental* 75 (2007) 210.
- [14] B.W.L. Southward, S. Basso, *SAE Technical Paper Series* 1 (2009) 239.
- [15] M. Valencia, E. López, S. Andrade, M.L. Iris, N. Guillén Hurtado, V. Rico Pérez, A. García García, C. Salinas Martínez de Leccea, A. Bueno-López, *Topics in Catalysis* 56 (2013) 452.
- [16] G. Mul, F. Kapteijn, C. Doornkamp, J.A. Moulijn, *Journal of Catalysis* 179 (1998) 258.
- [17] D. Reichert, H. Bockhorn, S. Kureti, *Applied Catalysis B: Environmental* 80 (2008) 248.
- [18] Z. Zhang, D. Han, S. Wei, Y. Zhang, *Journal of Catalysis* 276 (2010) 16.
- [19] S. Wagloehner, S. Kureti, *Applied Catalysis B: Environmental* 125 (2012) 158.
- [20] S. Wagloehner, S. Kureti, *Applied Catalysis B: Environmental* 129 (2013) 501.
- [21] S. Kureti, K. Hizbullah, W. Weisweiler, *Applied Catalysis B: Environmental* 3 (2003) 281.
- [22] M. Sander, A. Raj, O.R. Inderwildi, M. Kraft, S. Kureti, H. Bockhorn, *Carbon* 47 (2009) 866.
- [23] M. Mehring, M. Elsener, O. Kroecker, *ACS Catalysis* 2 (2012) 1507.
- [24] R. Matarrese, N. Artioli, L. Castoldi, L. Liotti, P. Forzatti, *Catalysis Today* 184 (2012) 271.
- [25] R.M. Cornell, U. Schwertmann, *The Iron Oxides*, Wiley-VCH Weinheim, 2003.
- [26] S.K. Saha, P. Pramanik, *Nanostructured Materials* 8 (1997) 29.
- [27] U.R.M. Schwertmann, Cornell, in: *Iron Oxides in the Laboratory*, Wiley-VCH, Weinheim, 1991.
- [28] S. Wagloehner, *Oxidation of Soot on Iron Oxide Catalysts*, Karlsruhe Institute of Technology, 2012 (Ph.D. Thesis).
- [29] H.M. Rietveld, *Acta Crystallographica* 22 (1967) 151.
- [30] P. Balle, H. Bockhorn, B. Geiger, N. Jan, S. Kureti, D. Reichert, T. Schröder, *Chemical Engineering and Processing* 45 (2006) 1065.
- [31] S. Wagloehner, D. Reichert, H. Bockhorn, S. Kureti, *Chemie Ingenieur Technik* 85 (2013) 686.
- [32] A.G. Konstantopoulos, M. Kostoglou, S. Lorentzo, N. Vlachos, *Catalysis Today* 188 2.
- [33] E.E. Unmuth, L.H. Schwartz, J.B. Butt, *Journal of Catalysis* 61 (1980) 242.
- [34] T. Finke, M. Gernsbeck, U. Eisele, C. Vincent, M. Hartmann, S. Kureti, H. Bockhorn, *Thermochimica Acta* 473 (2008) 32.
- [35] D. Klukowski, P. Balle, S. Wagloehner, S. Kureti, B. Kimmerle, A. Baiker, J.-D. Grunwaldt, *Applied Catalysis B: Environmental* 93 (2009) 185.
- [36] M. Weiss, G. Ertl, F. Nitschké, *Applications of Surface Science* 2 (1979) 614.
- [37] O. Hinrichsen, F. Rosowski, M. Muhler, G. Ertl, *Studies in Surface Science and Catalysis* 109 (1997) 389.
- [38] D. Reichert, T. Finke, N. Atanassova, H. Bockhorn, S. Kureti, *Applied Catalysis B: Environmental* 84 (2008) 803.
- [39] J.A. Kilner, R.A. De Souza, I.C. Fullarton, *Solid State Ionics* 703 (1996) 86–88.
- [40] M. Kisa, W.G. Stratton, T.K. Minton, K. van Benthem, S.J. Pennycook, P.M. Voyles, X. Chen, L. Li, J.C. Yang, *MRS Proceedings* 851 (2004) NN9.5.